



HAL
open science

[M16Ni24(CO)(40)](4-) Coinage Metal Tetrahedral Superatoms as Useful Building Blocks Related to Pyramidal Au-20 Clusters (M = Cu, Ag, Au). Electronic and Bonding Properties from Relativistic DFT Calculations

Franck Gam, Ramiro Arratia-Perez, Samia Kahlal, Jean-Yves Saillard, Alvaro Munoz-Castro

► **To cite this version:**

Franck Gam, Ramiro Arratia-Perez, Samia Kahlal, Jean-Yves Saillard, Alvaro Munoz-Castro. [M16Ni24(CO)(40)](4-) Coinage Metal Tetrahedral Superatoms as Useful Building Blocks Related to Pyramidal Au-20 Clusters (M = Cu, Ag, Au). Electronic and Bonding Properties from Relativistic DFT Calculations. *Journal of Physical Chemistry C*, 2018, 122 (8), pp.4723-4730. 10.1021/acs.jpcc.8b00227 . hal-01771101

HAL Id: hal-01771101

<https://univ-rennes.hal.science/hal-01771101>

Submitted on 26 Apr 2018

HAL is a multi-disciplinary open access archive for the deposit and dissemination of scientific research documents, whether they are published or not. The documents may come from teaching and research institutions in France or abroad, or from public or private research centers.

L'archive ouverte pluridisciplinaire **HAL**, est destinée au dépôt et à la diffusion de documents scientifiques de niveau recherche, publiés ou non, émanant des établissements d'enseignement et de recherche français ou étrangers, des laboratoires publics ou privés.

[M₁₆Ni₂₄(CO)₄₀]⁴⁺: Coinage Metal Tetrahedral Superatoms as Useful Building Blocks Related to Pyramidal Au₂₀ cluster (M = Cu, Ag, Au). Electronic and Bonding Properties from Relativistic DFT Calculations

Franck Gam^{a,b}, Ramiro Arratia-Perez^{a,}, Samia Kahlal^b, Jean-Yves Saillard^{b*} and Alvaro Muñoz-Castro^{c,*}*

^aDoctorado en Fisicoquímica Molecular, Universidad Andres Bello, República 275, Santiago, Chile

^bUMR-CNRS, 6226 "Institut des Sciences Chimiques de Rennes" Université de Rennes 1, 35042 Rennes Cedex (France).

^cLaboratorio de Química Inorgánica y Materiales Moleculares, Facultad de Ingeniería, Universidad Autónoma de Chile, El Llano Subercaseaux 2801, Santiago, Chile

Abstract

Characterization of the tetrahedral Au₂₀ structure in the gas-phase remains as a major landmark in gold cluster chemistry, where further efforts to stabilize this bare 20-electron superatom in solution, to extend and understand its chemistry have failed so far. Here, we account for the structural, electronic and bonding properties of [M₁₆Ni₂₄(CO)₄₀]⁴⁺ (M = Cu, Ag, Au) observed in solution for gold and silver. Our results show a direct electronic relationship with Au₂₀, owing that such species share a common tetrahedral [M₁₆]⁴⁺ central core with a 1S² 1P⁶ 1D¹⁰ 2S² jellium configuration. In the case of Au₂₀, the [Au₁₆]⁴⁺ core is capped by four Au⁺ ions, whereas in [M₁₆Ni₂₄(CO)₄₀]⁴⁺ it is capped by four Ni₆(CO)₁₀ units. In both cases, the capping entities are full part of the superatom entity where appears that the free (uncapped) [M₁₆]⁴⁺ species requires to be capped for further stabilization. It follows that the Ni₆(CO)₁₀ units in [M₁₆Ni₂₄(CO)₄₀]⁴⁺ should not be considered as external ligands as their bonding with the [M₁₆]⁴⁺ core is mainly associated with a delocalization of the 20 jellium electrons onto the Ni atoms. Thus, the [M₁₆Ni₂₄(CO)₄₀]⁴⁺ species can be seen as the solution version of tetrahedral M₂₀ clusters, encouraging experimental efforts to further develop the chemistry of such complexes as M(111) finite surface section structures, with M=Ag and Au and, and particularly promising with M=Cu. Furthermore, optical properties were simulated to assist future experimental characterization.

Introduction

Since the beginning of this century, the chemistry of ligand-protected Group 11 superatoms¹⁻³ has been tremendously developing, boosted in particular by the various potential applications of these atom- and electron-precise species.^{4,5} These clusters consist of a compact (generally pseudo-spherical) M_n core embedded in an outer protecting (“passivating”) shell made of various stabilizing ligands, such as for instance thiolates, halogenides and/or phosphines.^{2,5-8} In the specific case of thiolates, additional peripheral M(I) atoms are also present in the protecting shell, in which they occupy bridging positions between sulfur atoms. As a result, metal-thiolato “stapples” are formed, which are anchored to the M_n core through the coordination of sulfur.⁹⁻¹¹ Owing to the presence of formally anionic ligands on the outer shell, the inner metallic core is generally in a positive oxidation state ($[M_n]^{x+}$), giving rise to a non-integer averaged oxidation state $[(n - x)/n]$ lying between 0 and +1.

The stability of superatoms is associated with “magic” electron numbers which provide them with a closed-shell configuration. These “magic” electron counts (2, 8, 18, 20, 34, 40, 58...), can be rationalized within the framework of a spherical jellium-type model leading to one-electron cluster orbitals somehow resembling the atomic orbitals, called superatomic orbitals,^{5,12,13} and ordering as $1S < 1P < 1D < 2S < 1F < 2P < 1G \dots$ ^{1,6,12,14-17}

Interestingly, the naked neutral $[Au_{20}]$ tetrahedral cluster, obtained in the gas phase and further characterized by photoelectron spectroscopy,¹⁸ exhibits a closed-shell superatom configuration. It is characterized by a 20-electron “magic” number (the 5d(Au) electrons are not included in this counting). Its electronic structure, investigated by density functional calculations,¹⁸⁻²³ exhibits a large HOMO–LUMO energy gap, in agreement with its remarkable stability and unique optical and catalytic properties.^{18,24-30} Its structure is that of a bulk face-centered cubic (fcc) gold fragment, in a finite nanosized cluster motif.^{18,26}

Efforts to bring $[Au_{20}]$ species into solution has been carried out since the last ten years,^{26,31-35} which resulted in structures and electronic structures completely different from that of the bare $[Au_{20}]$ cluster. Interestingly, in the beginning of the 90’s, Dahl’s group reported the stabilization of an octahedral Au_6 core from the reaction between the Longoni–Chini $[Ni_3(CO)_6]^{2-}$ cluster³⁶ as reducing agent of a Au(I) solution. The resulting $[Au_6Ni_{12}(CO)_{24}]^{2-}$ cluster^{37,38} was a first example of the capability of Group 11 cores to be embedded in an outer shell made of organometallic units, which can increase the versatility of the protecting layer. Later, the same approach was extended to achieve high-nuclearity counterparts employing

1
2
3 Ag(OAc) and gold trichloride in modified conditions,³⁹ resulting in the formation of
4 $[\text{Ag}_{16}\text{Ni}_{24}(\text{CO})_{40}]^{4-}$ and $[\text{Au}_{16}\text{Ni}_{24}(\text{CO})_{40}]^{4-}$, respectively, with the former characterized via
5 single-crystal X-ray diffraction.³⁹
6

7
8 Both solid-state structures of $[\text{Au}_6\text{Ni}_{12}(\text{CO})_{24}]^{2-}$ and $[\text{Ag}_{16}\text{Ni}_{24}(\text{CO})_{40}]^{4-}$ exhibit an ideal
9 T_d symmetry. At first sight, they can be viewed as made of a superatomic core, ($[\text{Au}_6]^{2-}$ and
10 $[\text{Ag}_{16}]^{4-}$, respectively) covered by four approximatively planar $\text{Ni}_3(\text{CO})_6$ and $\text{Ni}_6(\text{CO})_{10}$ units,
11 respectively. However, a rationalization of the bonding between the superatom core and the
12 nickel carbonyl units is not as straightforward as for thiolate- or phosphine-covered
13 superatoms. Indeed, $[\text{:SR}]^-$ or :PR_3 are two-electron ligands, making localized 2-electron/2-
14 center bonds with the metal core. In $[\text{Ag}_{16}\text{Ni}_{24}(\text{CO})_{40}]^{4-}$ for example, each $\text{Ni}_6(\text{CO})_{10}$ units has
15 several bonding contacts with the cluster core (Figure 1), suggesting the possibility for
16 delocalized bonding. Moreover, it is likely that the electron-donation is going in the opposite
17 way as in the case of classical ligands, *i.e.*, from the core to the outer shell.⁴⁰ Therefore, the
18 question of the outer nickel carbonyl shell being not to be considered as a protecting ligand
19 but as a full part of the superatom entity arises. In any case, the role of the nickel carbonyl
20 units in the overall stabilization of these species is particularly puzzling. Although DFT
21 investigations of $[\text{Ag}_{16}\text{Ni}_{24}(\text{CO})_{40}]^{4-}$ by Walter have recently appeared,¹³ they were not
22 focused on the nature of the bonding between the nickel carbonyl groups and the Group 11
23 core, but to provide a analysis of the overall electronic structure.
24
25
26
27
28
29
30
31
32
33

34 Herein, we are interested in the role of the nickel carbonyl entity in the stabilization of
35 the whole cluster, extending the exploration along the Group 11 triad in the series
36 $[\text{M}_{16}\text{Ni}_{24}(\text{CO})_{40}]^{4-}$ ($\text{M} = \text{Cu}, \text{Ag}, \text{Au}$). Both electronic and structural features are rationalized
37 in terms of the superatom concept,^{6,10,13} showing a strong resemblance to the bare $[\text{Au}_{20}]$,
38 thus, proving that the synthesis in solution of a related passivated core is possible, which can
39 be useful for further explorations of its physico-chemical properties towards building blocks
40 for nanostructured materials.⁴¹ On the other hand, this allows the possibility to access towards
41 finite fcc fragments made of group 11 elements, for further understanding the size-dependent
42 behavior and properties of a few atoms section of group 11 $\text{M}(111)$ surfaces, which are
43 widely employed as active supporting surfaces.⁴²⁻⁴⁶
44
45
46
47
48
49
50
51
52
53
54
55
56
57
58
59
60

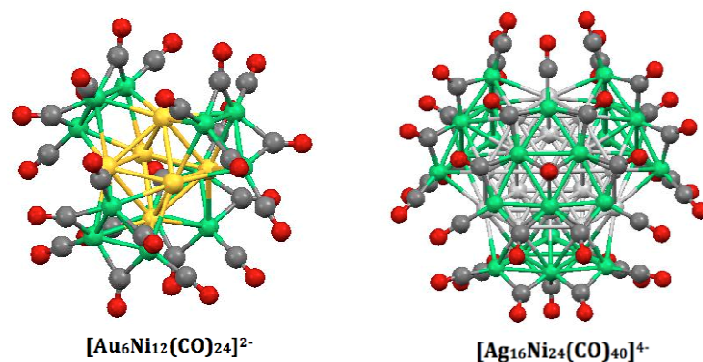


Figure 1. Molecular structure of $[\text{Au}_6\text{Ni}_{12}(\text{CO})_{24}]^{2-}$ (left) and $[\text{Ag}_{16}\text{Ni}_{24}(\text{CO})_{40}]^{4-}$ (right).

1. Computational details

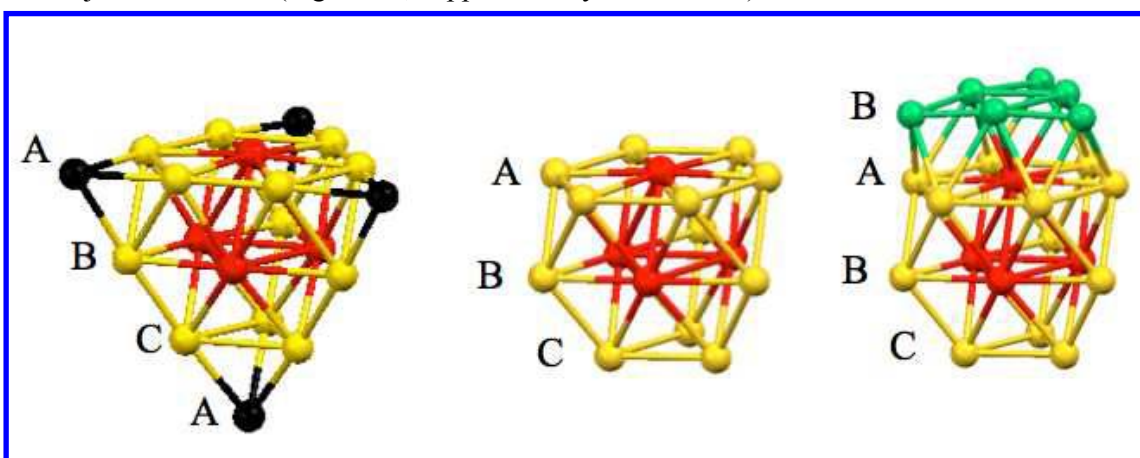
All density functional theory calculations were carried out by using the Amsterdam Density Functional (ADF) program⁴⁷ and the zeroth-order regular approximation (ZORA) was applied to incorporate scalar relativistic effects in our calculations. The triple- ζ Slater basis set was employed, plus two polarization functions (STO-TZ2P) for valence electrons, within the generalized gradient approximation (GGA) according to the Becke-Perdew (BP86) exchange functional.^{48,49} The frozen core approximation was applied to the $[1s^2-4f^{14}]$ inner electrons for Au, $[1s^2-4p^6]$ for Ag, $[1s^2-3p^6]$ for Cu, $[1s^2-3p^6]$ for Ni, $[1s^2]$ for C and $[1s^2]$ for O, leaving the remaining electrons to be treated variationally. A gradient convergence criterion of 10^{-5} and an energy convergence criterion of 10^{-8} were utilized to perform our geometry optimizations. Analyses of the interaction energy between fragments constituting the investigated clusters have been carried out within the Morokuma-Ziegler energy decomposition method.^{50–52} Time-dependent DFT (TD-DFT) calculations were employed at the same level, but using the Perdew-Burke-Ernzerhof (PBE) exchange-correlation functional⁵³ because offers a valuable comparison to the available computational calculation of UV-Vis spectrum for related clusters.^{4,54–57} It is worth mentioning that in the particular case of the investigated compounds, TD-DFT results at the BP86 level provided very similar results.

2. Results and discussions

2.1 The M_{16} core

In $[\text{Ag}_{16}\text{Ni}_{24}(\text{CO})_{40}]^{4-}$,³⁹ the T_d Ag_{16} core can be described in terms of two concentric shells, $\text{Ag}'_4@ \text{Ag}''_{12}$, with two types of symmetry-equivalent metals. As said above, it can also

1
 2
 3 be viewed as a compact piece taken out of an fcc metal. Indeed, along anyone of its four 3-
 4 fold axes, the packing goes in three successive compact planes, as sketched in Figure 2: A (7
 5 atoms), B (6 atoms) and C (3 atoms). Thus, the Ag_{16} core has four 7-atom and four 3-atom
 6 faces. In $[\text{Ag}_{16}\text{Ni}_{24}(\text{CO})_{40}]^{4+}$, each of the four 7-atom faces is capped by a $\text{Ni}_6(\text{CO})_{10}$ unit.
 7 Previous calculations by Walter¹³ lead to describe this cluster core as a 20-electron $[\text{Ag}_{16}]^{4+}$
 8 superatomic subsystem with the spherical jellium configuration $1\text{S}^2 1\text{P}^6 1\text{D}^{10} 2\text{S}^2$. At this
 9 point of the discussion, one should remind that in this type of clusters, only the 5s(Ag)
 10 electrons are considered participating to the bonding within the superatom core, and
 11 consequently to the jellium electron count. The fully occupied 4d(Ag) levels remain basically
 12 non-bonding and low-lying. Then the similarity between the $[\text{Ag}_{16}]^{4+}$ subsystem and $[\text{Ag}_{20}]$ (or
 13 $[\text{Au}_{20}]$) are striking. Indeed, the neutral unligated 20-electron $[\text{Ag}_{20}]$ (or $[\text{Au}_{20}]$)^{18,21,23} adopts a
 14 tetrahedral structure that can be generated from the $[\text{Ag}_{16}]^{4+}$ subsystem by capping its four
 15 triangular faces with four Ag^+ . In these $[\text{M}_{20}]$ superatoms, the compact plane stacking goes as
 16 A (7 atoms), B (6 atoms), C (3 atoms) and A (1 atom). The alternative description of $[\text{M}_{20}]$ in
 17 terms of concentric shells, $\text{M}'_4@\text{M}''_{12}@\text{M}'''_4$, reveals three types of symmetry-equivalent
 18 metals.²² We have optimized the T_d - $[\text{M}_{16}]^{4+}$ and T_d - $[\text{M}_{20}]$ (M = Cu, Ag, Au) species assuming
 19 T_d symmetry and found them to be closed-shell minima in these spatial configurations. Their
 20 major computed results are provided in Table S1. The relationship between their 20-electron
 21 superatom electron configurations is evidenced by the plots of the $[\text{Ag}_{16}]^{4+}$ and $[\text{Ag}_{20}]$ Kohn-
 22 Sham jellium orbitals (Figure S1, supplementary information).
 23
 24
 25
 26
 27
 28
 29
 30
 31
 32
 33
 34



49
 50 Figure 2. Illustration of the fcc packing (A, B and C planes) in Ag_{20} (left) and the Ag_{16} core of
 51 $[\text{Ag}_{16}\text{Ni}_{24}(\text{CO})_{40}]^{4+}$ (middle) and with one Ni_6 plane (right). The red, yellow and black colors
 52 correspond to the symmetry-equivalent Ag' , Ag'' and Ag''' atoms, respectively, in Ag_{20}
 53 ($\text{Ag}'_4@\text{Ag}''_{12}@\text{Ag}'''_4$) and the Ag_{16} core ($\text{Ag}'_4@\text{Ag}''_{12}$). The green color corresponds to Ni.
 54
 55
 56
 57
 58
 59
 60

1
2
3 A Morokuma-Ziegler decomposition of the bonding energy⁵⁰⁻⁵² between the $[M_{16}]^{4+}$
4 core and its $[M_4]^{4+}$ envelope in the $[M_{20}]$ equilibrium geometry has been performed (see
5 Computational Details) and its components are given in Table 1. For the three metals, the total
6 bonding energy between the two fragments is negative (stabilizing), with similar values for M
7 = Cu and Au, whereas that corresponding to Ag is weaker. This is in phase with the computed
8 cohesion energy of $[M_{20}]$ (Table S1, supplementary information) and with previous
9 calculations on bare Group 11 metal clusters.⁵⁸ In fact, in such bare metal clusters Ag behaves
10 always a bit differently than Cu and Ag, because the periodical trend is likely to be
11 counterbalanced by the relativistic effects.⁵⁸ Among the three components of the bonding
12 energy, the Pauli repulsion is, by nature, positive. On the other hand, the two other
13 components (electrostatic and orbital interactions) are stabilizing and more or less follow the
14 same trend as the total bonding energy. The a_1 and t_2 components are dominating the orbital
15 interaction energy. They result from the participation to the bonding of the valence $(n + 1)s$
16 orbitals of M^+ , with some $(n + 1)p_\sigma$ contribution. Indeed, within the cluster T_d symmetry, the
17 four valence s-type AOs combine into $a_1 + t_2$ and interact strongly with their 2S (a_1) and 1D (t_2)
18 counterparts on the $[M_{16}]^{4+}$ fragment. As a consequence, the occupation after
19 interaction of the M^+ $(n + 1)s$ orbital is substantial (~ 1.0 e, see Table 1), whereas that of its $(n$
20 $+ 1)p_\sigma$ AO remains lower than 0.1 e in the three clusters. The less important e and t_1
21 contributions of the orbital interaction energy (Table 1), as well as the $(n + 1)p$ and nd
22 populations of the capping atoms, are the trace of some bonding interaction of the M^+ vacant
23 $(n + 1)p_\pi$ combinations ($e + t_1 + t_2$) with occupied $[M_{16}]^{4+}$ counterparts, as well as of the M^+ nd
24 occupied combinations ($a_1 + 2e + 2t_1 + 3t_2$) with some vacant $[M_{16}]^{4+}$ MOs. In any case, the
25 participation of the M^+ $(n + 1)p$ and nd AOs in the bonding with the $[M_{16}]^{4+}$ core remains
26 minor.
27
28
29
30
31
32
33
34
35
36
37
38
39
40
41
42
43

44 Table 1. Decomposition of the bonding energy between the $[M_{16}]^{4+}$ core and its outer capping
45 $[M_4]^{4+}$ fragment in the $[M_{20}]$ ($M = Cu, Ag, Au$) clusters of T_d symmetry and electron
46 configuration of the four capping atoms. All energies are in eV.

Compound (T_d)	$[Cu_{20}]$		$[Ag_{20}]$		$[Au_{20}]$	
Fragmentation	$[Cu_{16}]^{4+} + [Cu_4]^{4+}$		$[Ag_{16}]^{4+} + [Ag_4]^{4+}$		$[Au_{16}]^{4+} + [Au_4]^{4+}$	
Pauli repulsion	23.30		21.13		30.66	
Electrostatic interaction	-72.60		-64.79		-75.02	
Orbital interaction decomposition	a_1	-4.24	a_1	-3.87	a_1	-5.63
	a_2	-0.01	a_2	-0.01	a_2	-0.02
	e	-1.41	e	-1.00	e	-1.23
	t_1	-1.38	t_1	-0.89	t_1	-2.05

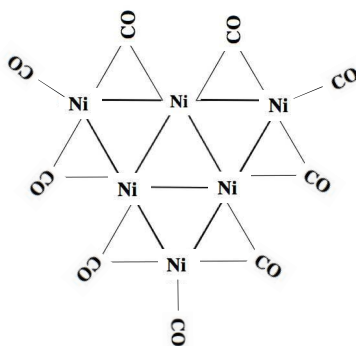
1
2
3
4
5
6
7
8
9
10
11
12
13
14
15
16
17
18
19
20
21
22
23
24
25
26
27
28
29
30
31
32
33
34
35
36
37
38
39
40
41
42
43
44
45
46
47
48
49
50
51
52
53
54
55
56
57
58
59
60

	t_2	-9.33	t_2	-8.40	t_2	-12.45
Total orbital interaction		-16.38		-14.17		-21.38
Total bonding energy		-65.68		-57.83		-65.75
Jellium electron configuration of the $[M_{16}]^{4+}$ fragment		$1S^{1.95} 1P^{5.79} 1D^{7.83} 2S^{0.79} 2P^{0.24}$ $1F^{0.53}$		$1S^{1.98} 1P^{5.94} 1D^{7.36} 2S^{0.71} 2P^{0.09}$ $1F^{0.37}$		$1S^{1.95} 1P^{5.91} 1D^{7.74} 2S^{0.56} 2P^{0.12}$ $1F^{0.76}$
Electron configuration of the outer capping atoms		$3d^{9.81} 4s^{0.93} 4p^{0.22}$		$4d^{9.89} 5s^{0.96} 5p^{0.14}$		$5d^{9.71} 6s^{1.14} 6p^{0.19}$

2.2 The Protecting $\text{Ni}_6(\text{CO})_{10}$ units

Being centered on a C_3 axis of the tetrahedral $[\text{M}_{16}\text{Ni}_{24}(\text{CO})_{40}]^{4+}$ cluster (Figure 1), each of the four $\text{Ni}_6(\text{CO})_3(\mu\text{-CO})_6(\mu_3\text{-CO})$ units has local C_{3v} symmetry. In fact, one can view the nickel atoms as part of the whole metal compact packing of the cluster (Figure 2, right side), which, along each of the C_3 axis goes as C (M_3), B (M_6), A (M_7) and B (Ni_6). If, in a first step, we do not consider the central μ_3 -carbonyl ligand, the remaining $\text{Ni}_6(\text{CO})_9$ fragment is almost planar, of idealized D_{3h} symmetry (Scheme 1). This approximately planar $\text{Ni}_6(\text{CO})_9$ neutral fragment has $(6 \times 10) + (9 \times 2) = 78$ electrons in the metal coordination environment. This is the electron count that one would predict at first sight, assuming a localized 2-electron/2-center bonding scheme (nine 2-electron Ni-Ni bonds), with the six in-plane coordinated metals satisfying the 16-electron rule $[(6 \times 16) - (2 \times 9) = 78]$. However, it appears from the nearly planar 6-fold connectivity of the three inner Ni atoms (Scheme 1) that a localized bonding scheme with 9 Ni-Ni bonds does not apply properly. Indeed, the inner Ni atoms have only 5 in-plane valence orbitals (s, p_x , p_y , $d_{x^2-y^2}$ and d_{xy}) available for making 6 “bonds”. Considering that the metal $d_{x^2-y^2}$ and d_{xy} AOs are participating in 6 among the 12 Ni-(μ -CO) bonds (those involving the $\pi^*(\text{CO})$ orbitals) and in all the Ni-Ni bonds, one is left with $(6 \times 2) - 6 = 6$ localized 2-electron/2-center Ni-Ni bonds. A reasonable Lewis description of the $\text{Ni}_6(\text{CO})_9$ fragment would be to discard the three central Ni-Ni bonds in Scheme 1. This would leave the three inner metals with a 14-electron configuration, whereas the three outer ones would remain 16-electron centers. This electron-deficient and delocalized situation makes this $\text{Ni}_6(\text{CO})_9$ fragment somewhat different from structurally related species, such as $[\text{Pt}_3\text{Fe}_3(\text{CO})_{15}]^{0/-2-}$, for example.⁵⁹⁻⁶²

Adding now an out-of-plane μ_3 -CO on the central metal triangle of $\text{Ni}_6(\text{CO})_9$ to complete the full $\text{Ni}_6(\text{CO})_{10}$ organometallic unit reduces the electron deficiency of this triangle by 2 electrons and orientates the associated electron-accepting ability to the other side of the Ni_6 plane.



Scheme 1. Connectivity within a $\text{Ni}_6(\text{CO})_3(\mu\text{-CO})_6$ fragment in $[\text{Ag}_{16}\text{Ni}_{24}(\text{CO})_{40}]^{4-}$.

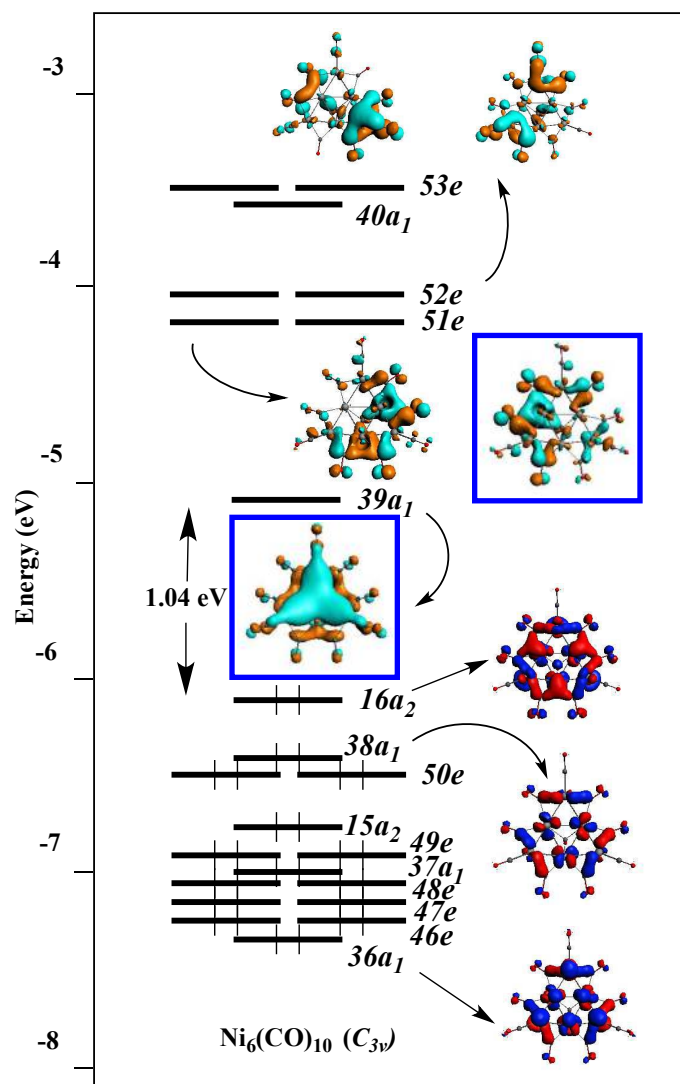


Figure 3. Kohn-Sham orbital diagram of free $\text{Ni}_6(\text{CO})_3(\mu\text{-CO})_6(\mu_3\text{-CO})$ (C_{3v} symmetry).

1
2
3 The optimized geometry of the free $\text{Ni}_6(\text{CO})_{10}$ unit (assuming C_{3v} symmetry) and its
4 Kohn-Sham MO diagram are shown in Figure 3. Its moderate out-of-planarity allows
5 strengthening a bit the bonding around the metal centers by somewhat reducing their electron
6 deficiency. The Ni-Ni bond lengths, 2.594 Å (inner) and 2.431 Å (peripheral) are consistent
7 with the above qualitative description of the bonding. The electron deficiency is evidenced by
8 the existence of low-lying vacant orbitals. In particular the $39a_1$ LUMO has significant in-
9 phase metal $4p_z$ AO's. The $16a_2$ HOMO has in-plane 3d-type character, whereas the $38a_1$
10 HOMO-1 is a $3d_{z^2}$ combination, as well as the low-lying $36a_1$. Contrarily to the HOMO, these
11 two last occupied MOs have favorable directional properties to interact with the $[\text{M}_{16}]^{4+}$ core.
12
13
14
15
16
17
18

19 **2.3 Interaction of a single $\text{Ni}_6(\text{CO})_{10}$ with the $[\text{M}_{16}]^{4+}$ core**

20 The best way to analyze the role played by the outer organometallic shell in the bonding
21 and stability of $[\text{M}_{16}(\text{Ni}_{24}(\text{CO})_{40})]^{4+}$ is to first consider the interaction between one $\text{Ni}_6(\text{CO})_{10}$
22 fragment and the $[\text{M}_{16}]^{4+}$ core. In this respect, we have undertaken a Morokuma-Ziegler
23 decomposition of the bonding energy⁵⁰⁻⁵² between the $[\text{M}_{16}]^{4+}$ and $\text{Ni}_6(\text{CO})_{10}$ fragments in an
24 $[\text{M}_{16}(\text{Ni}_6(\text{CO})_{10})]^{4+}$ model of C_{3v} symmetry, the structure of which (single-point calculation)
25 being taken out of the optimized geometry of the $[\text{M}_{16}(\text{Ni}_{24}(\text{CO})_{40})]^{4+}$ tetrahedral parent. Its
26 components are given in Table 2. For the three models, the orbital interaction energy is
27 dominated by its a_1 and e components, in agreement with the fact that the directional
28 properties of the $\text{Ni}_6(\text{CO})_{10}$ orbitals of a_2 symmetry are unfavorable. Moreover, an analysis of
29 the fragment orbital populations after interaction indicates that the $[\text{M}_{16}]^{4+}$ orbitals which are
30 by far the most involved in the interaction are those which can be identified as the jellium-
31 type MOs (Figure S1). Among them, the 1D and 2S orbitals, which are occupied in the
32 isolated $[\text{M}_{16}]^{4+}$, are dominating the interaction (see their population in the $[\text{M}_{16}(\text{Ni}_6(\text{CO})_{10})]^{4+}$
33 model in Table 2), whereas the 2P and 1F orbitals (lowest vacant levels in $[\text{M}_{16}]^{4+}$) interact in
34 a lesser extent. Consistently, an examination of the occupation of the $\text{Ni}_6(\text{CO})_{10}$ fragment after
35 interaction (Table 2) indicates a major role played by the five lowest unoccupied
36 organometallic MOs, in particular the $39a_1$ LUMO and the $51e$ LUMO+1 which are acting as
37 strong accepting orbitals. The organometallic donor orbitals are principally of a_1 symmetry
38 (d_{z^2} combinations) and much less efficient. Thus, the $\text{Ni}_6(\text{CO})_{10}$ acts mainly as a strong
39 electron acceptor, as exemplified by its largely negative charge in the computed model (Table
40 2). Moreover, its frontier orbitals interact mostly with the jellium-type orbitals of $[\text{M}_{16}]^{4+}$ core.
41
42
43
44
45
46
47
48
49
50
51
52
53
54
55
56
57
58
59
60

electron donor and interact with core surface orbitals, different from the delocalized jellium-type ones. Rather, the interaction of the $\text{Ni}_6(\text{CO})_{10}$ fragment with the $[\text{M}_{16}]^{4+}$ core resembles that of the four outer capping M^+ atoms in the $[\text{M}_{20}]$ clusters (see above), despite of the fact they cap different faces of the $[\text{M}_{16}]^{4+}$ core.

Table 2. Decomposition of the bonding energy between the $[\text{M}_{16}]^{4+}$ and $\text{Ni}_6(\text{CO})_{10}$ fragment in the C_{3v} model $[\text{M}_{16}(\text{Ni}_6(\text{CO})_{10})]^{4+}$ ($\text{M} = \text{Cu}, \text{Ag}, \text{Au}$) and population analysis of the fragment. All energies are in eV.

Compound (C_{3v})	$[\text{Cu}_{16}\text{Ni}_6(\text{CO})_{10}]^{4+}$		$[\text{Ag}_{16}\text{Ni}_6(\text{CO})_{10}]^{4+}$		$[\text{Au}_{16}\text{Ni}_6(\text{CO})_{10}]^{4+}$	
Fragmentation	$[\text{Cu}_{16}]^{4+} + \text{Ni}_6(\text{CO})_{10}$		$[\text{Ag}_{16}]^{4+} + \text{Ni}_6(\text{CO})_{10}$		$[\text{Au}_{16}]^{4+} + \text{Ni}_6(\text{CO})_{10}$	
Pauli repulsion	31.57		24.90		26.17	
Electrostatic interaction	-29.87		-23.24		-24.21	
Orbital interaction decomposition	a_1	-5.34	a_1	-4.71	a_1	-4.43
	a_2	-0.52	a_2	-0.42	a_2	-0.72
	e	-7.90	e	-6.33	e	-6.69
Total orbital interaction	-13.77		-11.46		-11.85	
Total bonding energy	-12.09		-9.79		-9.89	
Jellium electron configuration of the $[\text{M}_{16}]^{4+}$ fragment	$1\text{S}^{1.88} 1\text{P}^{5.83} 1\text{D}^{8.78} 2\text{S}^{1.49} 2\text{P}^{0.28} 1\text{F}^{0.63}$		$1\text{S}^{1.90} 1\text{P}^{5.58} 1\text{D}^{8.52} 2\text{S}^{1.53} 2\text{P}^{0.27} 1\text{F}^{0.48}$		$1\text{S}^{1.90} 1\text{P}^{5.95} 1\text{D}^{9.02} 2\text{S}^{1.64} 2\text{P}^{0.48} 1\text{F}^{0.48}$	
Occupation of selected $\text{Ni}_6(\text{CO})_{10}$ frontier MOs	$(36a_1)^{1.90} (38a_1)^{1.85} (16a_2)^{1.92} (39a_1)^{1.17} (51e)^{1.12} (52e)^{0.36}$		$(36a_1)^{1.87} (38a_1)^{1.88} (16a_2)^{1.92} (39a_1)^{1.22} (51e)^{1.02} (52e)^{0.36}$		$(36a_1)^{1.88} (38a_1)^{1.79} (16a_2)^{1.86} (39a_1)^{1.02} (51e)^{0.82} (52e)^{0.40}$	
$\text{Ni}_6(\text{CO})_{10}$ Mulliken charge	-1.64		-1.84		-1.43	

2.4 The $[\text{M}_{16}(\text{Ni}_{24}(\text{CO})_{40})]^{4+}$ clusters

The geometries of the $[\text{M}_{16}(\text{Ni}_{24}(\text{CO})_{40})]^{4+}$ ($\text{M} = \text{Cu}, \text{Ag}, \text{Au}$) clusters have been fully optimized (see computational details). Major structural data are provided in Table 3, together with the computed HOMO-LUMO gaps which are consistent with their closed-shell superatom nature. The optimized distances of the silver species are in good agreement with the reported corresponding experimental values.³⁹

Table 3. Relevant computed data for $[\text{M}_{16}\text{Ni}_{24}(\text{CO})_{40}]^{4+}$ ($\text{M} = \text{Cu}, \text{Ag}, \text{Au}$) clusters. $\Delta E_{\text{H-L}}$ is HOMO-LUMO gap in eV. The two types of symmetry-equivalent group 11 atoms refer to the concentric spheres $\text{M}'_4@M''_{12}$ (see Section 3.1). The two types of symmetry equivalent Ni atoms are labeled Ni_A and Ni_B , the inner and outer metals in $\text{Ni}_6(\text{CO})_{10}$, respectively (see Section 3.2). Distances are given in Å. Experimental values of Dahl's silver cluster taken from Ref.³⁹ are given in parenthesis.

T_d	$[\text{M}'_4@M''_{12}@ \{\text{Ni}_{24}(\text{CO})_{40}\}]^{4+}$
-------	---

	ΔE_{H-L}	M'-M'	M'-M''	M''-M''	M'-Ni _A	M''-Ni _A	M''-Ni _B	Ni _A -Ni _A	Ni _A -Ni _B
[Cu ₁₆ Ni ₂₄ (CO) ₄₀] ⁴⁺	1.06	2.625	2.493	2.481-2.503	2.681	2.652	2.558	2.703	2.446
[Ag ₁₆ Ni ₂₄ (CO) ₄₀] ⁴⁺	0.83	2.995 (2.97)	2.865 (2.83)	2.832-2.897 (2.84)	2.838 (2.80)	2.973 (2.93)	2.731 (2.69)	2.703 (2.67)	2.449 (2.42)
[Au ₁₆ Ni ₂₄ (CO) ₄₀] ⁴⁺	0.88	3.067	2.872	2.847-2.893	2.780	2.935	2.699	2.743	2.485

Table 4. Decomposition of the bonding energy between the [M₁₆]⁴⁺ core its [Ni₂₄(CO)₄₀] envelope in the T_d [M₁₆(Ni₂₄(CO)₄₀)]⁴⁺ (M = Cu, Ag, Au) and population analysis of the fragment. All energies are in eV.

Compound (T _d)	[Cu ₁₆ Ni ₂₄ (CO) ₄₀] ⁴⁺		[Ag ₁₆ Ni ₂₄ (CO) ₄₀] ⁴⁺		[Au ₁₆ Ni ₂₄ (CO) ₄₀] ⁴⁺	
Fragmentation	[Cu ₁₆] ⁴⁺ + [Ni ₆ (CO) ₁₀] ₄		[Ag ₁₆] ⁴⁺ + [Ni ₆ (CO) ₁₀] ₄		[Au ₁₆] ⁴⁺ + [Ni ₆ (CO) ₁₀] ₄	
Pauli repulsion	132.40		99.99		109.23	
Electrostatic interaction	-125.13		-94.39		-102.49	
Orbital interaction decomposition	a ₁	-6.52	a ₁	-5.22	a ₁	-4.65
	a ₂	-0.26	a ₂	-0.21	a ₂	-0.27
	e	-8.51	e	-6.84	e	-6.35
	t ₁	-7.53	t ₁	-5.16	t ₁	-8.05
	t ₂	-25.62	t ₂	-22.36	t ₂	-21.94
Total orbital interaction	-48.44		-39.78		-41.26	
Total bonding energy	-48.45		-34.18		-34.51	
Ni ₆ (CO) ₁₀ Mulliken charge	-1.68		-1.57		-1.12	

The Morokuma-Ziegler bonding energy decomposition⁵⁰⁻⁵² between the [M₁₆]⁴⁺ core and its complete [Ni₂₄(CO)₄₀] envelope is provided in Table 4. Both total bonding energy and its orbital component indicate stronger interaction with copper, whereas silver and gold behave similarly. The a₁, e, t₁ and (overall) t₂ components of the orbital interaction energy are dominating. From the results obtained on the [M₁₆(Ni₆(CO)₁₀)]⁴⁺ model (see above), one can deduce that they result mainly from the participation of the p_z and d₂₂ combinations of the individual [Ni₆(CO)₁₀] units (a₁ and e in local C_{3v} symmetry). From the jellium electron configuration of the [M₁₆]⁴⁺ and from the occupation of the frontier orbitals of a single Ni₆(CO)₁₀ fragment in the [M₁₆(Ni₂₄(CO)₄₀)]⁴⁺ cluster, it appears clearly that the major interactions between the [M₁₆]⁴⁺ core and its [Ni₂₄(CO)₄₀] envelope involves the occupied core jellium orbitals on one side and the accepting π-type orbitals (of substantial p_z character) of the [Ni₆(CO)₁₀] unit on the other side. This result confirms that the behavior of the [Ni₂₄(CO)₄₀] envelope is not that of a “passivating” ligand shell, but rather of a full part of the superatomic entity.

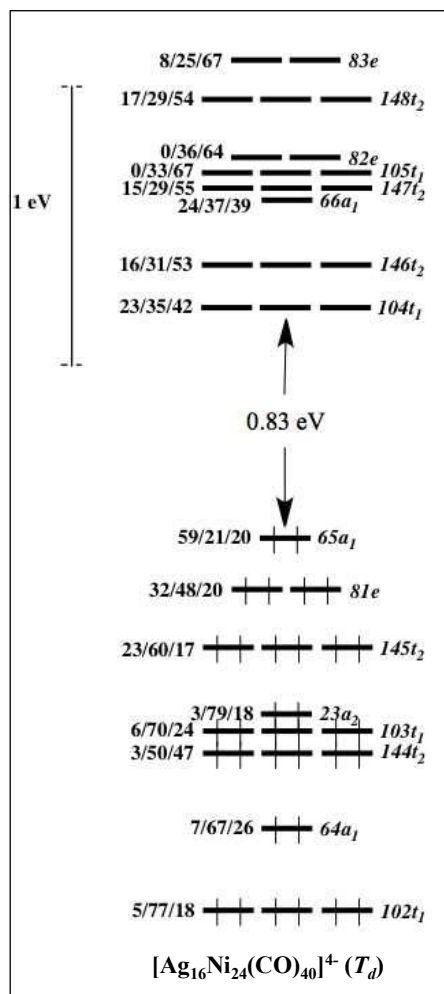


Figure 4. Kohn-Sham orbital diagram of $[\text{Ag}_{16}\text{Ni}_{24}(\text{CO})_{40}]^{4+}$. The MO localization (in %) is given as follows: $\text{Ag}_{16}/\text{Ni}_{24}/(\text{CO})_{40}$.

The Kohn-Sham MO diagram of $[\text{Ag}_{16}\text{Ni}_{24}(\text{CO})_{40}]^{4+}$ is shown in Figure 4. Those of the Cu and Au relatives (not shown) are similar. The highest occupied levels can be assimilated to the 2S ($65a_1$) and 1D ($81e$ and $145t_2$) jellium levels. The lowest unoccupied levels correspond to a mixture of the 1F and 2P jellium orbitals with $\pi^*(\text{CO})$ combinations.

2.5 Optical properties

From the heterometallic nature of the title clusters, interesting optical properties may be anticipated. This is why a TD-DFT analysis has been undertaken in order to simulate their UV-vis spectra which are shown in Figure 5 allowing estimating characteristic patterns for further possible experimental realization. They exhibit similar features with four major absorption bands. The relevant associated electronic transitions are listed in Table 5 in the case of $M = \text{Ag}$. One can see that all the relevant transitions have a MLCT character

$[M_{16}(Ni_{24}(CO)_{40})]^{4-}$ ($M = Cu, Ag, Au$) clusters. The low-energy transitions are also associated with some core-ligand charge transfer character. The results, shows a sizable blue-shift of the main peaks for $[Au_{16}Ni_{24}(CO)_{40}]^{4-}$ in relation to its copper and silver counterparts, revealing strong differences between the expected optical patterns along the series.

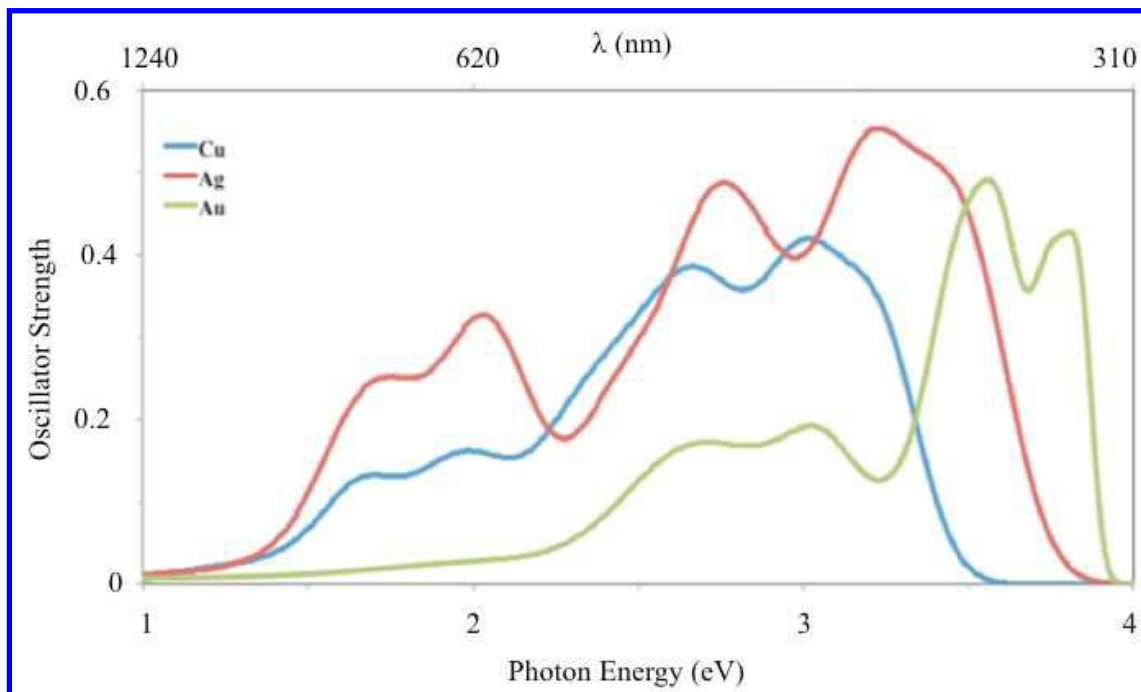


Figure 5. TD-DFT-simulated UV-vis absorption spectra of $[M_{16}Ni_{24}(CO)_{40}]^{4-}$ ($M=Cu, Ag$ and Au).

Table 5. Major computed electronic absorption for $[Ag_{16}Ni_{24}(CO)_{40}]^{4-}$. The MO localizations (in %) are given in parentheses as follows: $Ag_{16}/Ni_{24}/(CO)_{40}$.

Photon Energy (eV) ^a	%	Major components of the transition
1.70 (0.13)	26	$145t_2$ (23/60/17) \rightarrow $66a_1$ (24/37/39)
	13	$65a_1$ (59/21/20) \rightarrow $148t_2$ (17/29/54)
2.02 (0.11)	23	$102t_1$ (5/77/18) \rightarrow $104t_1$ (23/35/42)
	22	$81e$ (32/48/20) \rightarrow $148t_2$ (17/29/54)
	15	$144t_2$ (3/50/47) \rightarrow $105t_1$ (0/33/67)
	12	$103t_1$ (6/70/24) \rightarrow $82e$ (0/36/64)
2.72 (0.09)	27	$142t_2$ (8/83/9) \rightarrow $147t_2$ (15/29/55)
	26	$76e$ (4/86/10) \rightarrow $104t_1$ (23/35/42)

3.23 (0.06)	21	$134t_2 (7/85/6) \rightarrow 146t_2 (16/31/53)$
	18	$142t_2 (8/83/9) \rightarrow 83e (8/25/67)$
	13	$97t_1 (4/91/5) \rightarrow 82e (0/36/64)$

^a Values in parenthesis correspond to oscillator strengths in a.u..

2.6 Bonding Considerations

So far, the closed-shell 20-electron $[M_{16}]^{4-}$ superatom has not been reported, even as a ligand-passivated species, and one may wonder whether it is sufficiently stable for being isolated. Indeed, apart from its somewhat large negative charge, its 2S HOMO contains an antibonding interaction between the M_4 inner core and its outer M_{12} cage, depicting a radial node. Despite its bonding nature within each individual M_4 and M_{12} sphere, this orbital is likely lacking bonding character. A way to reinforce the 2S bonding is to add a third concentric sphere, made of 0-electron capping units having empty σ -type frontier orbitals, the in-phase combination of which being able to stabilize the 2S HOMO, whereas in addition the other combinations would also contribute to somewhat stabilize the 1D and 1P orbitals. This is what happens in $[M_{20}]$ ($M'_4 @ M''_{12} @ M_4'''$), but also in $[M_{16}Ni_{24}(CO)_{40}]^{4-}$ ($[M'_4 @ M''_{12} @ \{Ni_{24}(CO)_{40}\}]^{4-}$). In the latter cluster, the four $Ni_6(CO)_{10}$ fragment, which pack to the M_{16} core in a compact fashion, are mainly interacting with the occupied jellium orbitals by using their vacant σ -type frontier orbitals. This behavior is different from that of a 2-electron ligand (thiolate, halogenide, phosphine, etc...) which is expected to have its occupied frontier orbital to interact with a core-accepting orbital localized on the superatom surface. Both situations are sketched in a schematic manner in Figure 6. Although very simplified, this description illustrates most of the differences between ligands and outer fragments belonging to the superatom core. The real situation is of course somehow more complex. In particular, significant mixing often occurs between the surface accepting orbitals of the superatomic core and the vacant antibonding jellium-type orbitals, which makes the distinction between them difficult. This is what happens for 1F and 2P MOs of the $[M_{16}]^{4-}$ cores considered in this paper, which exhibit more accepting character than expected at first sight. Also, secondary bonding interactions occur between occupied MOs (mainly jellium-type) of the jellium core and vacant p-type of the supplementary superatom fragment.

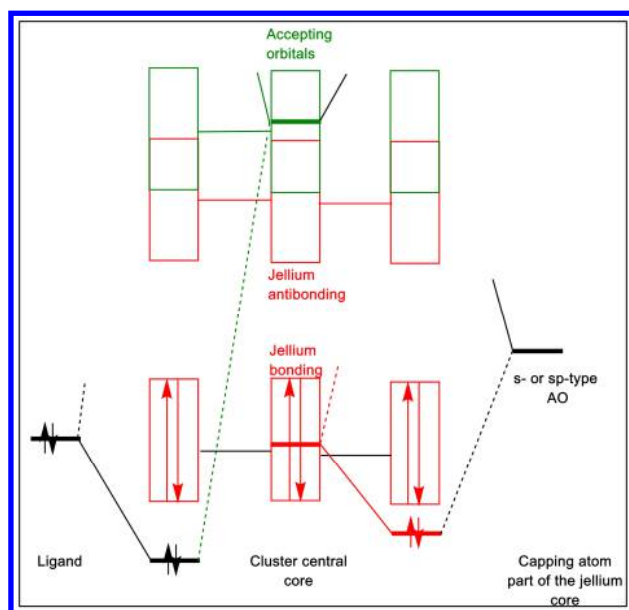


Figure 6. Simplified MO interaction diagram illustrating the difference between an outer sphere atom belonging to the superatom entity (right side) and a (neutral or anionic) 2-electron ligand (left side).

Conclusions

In summary, our calculations indicate that $[\text{Ag}_{16}\text{Ni}_{24}(\text{CO})_{40}]^{4-}$ and $[\text{Au}_{16}\text{Ni}_{24}(\text{CO})_{40}]^{4-}$ are strongly related to bare tetrahedral Ag_{20} and Au_{20} clusters, showing a $1\text{S}^21\text{P}^61\text{D}^{10}2\text{S}^2$ closed-shell configuration. In addition, the $[\text{Cu}_{16}\text{Ni}_{24}(\text{CO})_{40}]^{4-}$ counterparts is shown to be thermodynamically more stable than its Ag and Au relatives, thus, it should be possible to characterize it experimentally, similarly to its silver and gold counterparts. Hence, the in-solution stabilization of the inner FCC-like M_{16} kernel motif as basic structure observed in the Au_{20} golden pyramid, allows to further explore the physico-chemical characteristics towards tetrahedral building blocks for nanostructured materials with novel properties. In addition, such structures represent a minimal model of four faces representing a (111) surface of a face-centered cubic unit cell in order to study catalytic activity, among other properties. We envisage versatile chemistry on the basis of the potential modifications in the surface of the M_{16} core.

ASSOCIATED CONTENT

Supporting Information

1
2
3 Relevant computed data for $[M_{16}]^{4+}$ and $[M_{20}]$ clusters (M=Cu, Ag, Au) of
4 jellium configuration $1S^2 1P^6 1D^{10} 2S^2$, and Kohn-Sham jellium orbitals of
5 $[Au_{16}]^{4+}$ and $[Au_{20}]$. Major electronic absorption for $[M_{16}Ni_{24}(CO)_{40}]^{4+}$ (M = Cu,
6 Ag, Au) computed at the PBE and BP86 levels. This material is available free of
7 charge via the Internet at <http://pubs.acs.org>.
8
9

10 11 12 **AUTHOR INFORMATION**

13 14 **Corresponding Author**

15
16 Ramiro Arratia-Perez*
17 rarratia@unab.cl
18

19
20 Jean-Yves Saillard*
21 jean-yves.saillard@univ-rennes1.fr
22

23
24 Alvaro Muñoz-Castro*
25 alvaro.munoz@uautonoma.cl
26

27 28 **Author Contributions**

29
30 The manuscript was written through contributions of all authors.
31

32 33 **Acknowledgement**

34
35 The authors thank the financial support from FONDECYT 1140359, 1150629, and
36 MILLENNIUM project RC120001 grants. The GENCI French national computer resource is
37 acknowledged (grant a0010807367). This research has been performed as part of the Chilean-
38 French International Associated Laboratory for “Multifunctional Molecules and Materials”
39 (LIA-CNRS N°1027). F.G. thanks the Région Bretagne (ARED NANOCLU) and the
40 University Andres Bello for a joint PhD studentship.
41
42
43
44
45
46
47
48
49
50
51
52
53
54
55
56
57
58
59
60

References

- (1) Jena, P. Beyond the Periodic Table of Elements: The Role of Superatoms. *J. Phys. Chem. Lett.* **2013**, *4*, 1432–1442.
- (2) Claridge, S. A.; Castleman, A. W.; Khanna, S. N.; Murray, C. B.; Sen, A.; Weiss, P. S. Cluster-Assembled Materials. *ACS Nano* **2009**, *3*, 244–255.
- (3) Jena, P.; Khanna, S. N.; Rao, B. K. *Clusters and Nano-Assemblies: Physical and Biological Systems*; World Scientific, 2005.
- (4) Jiang, D. The Expanding Universe of Thiolated Gold Nanoclusters and Beyond. *Nanoscale* **2013**, *5*, 7149–7160.
- (5) Walter, M.; Akola, J.; Lopez-Acevedo, O.; Jadzinsky, P. D.; Calero, G.; Ackerson, C. J.; Whetten, R. L.; Gronbeck, H.; Hakkinen, H. A Unified View of Ligand-Protected Gold Clusters as Superatom Complexes. *Proc. Natl. Acad. Sci.* **2008**, *105*, 9157–9162.
- (6) Castleman, A. W.; Khanna, S. N. Clusters, Superatoms, and Building Blocks of New Materials. *J. Phys. Chem. C* **2009**, *113*, 2664–2675.
- (7) Jadzinsky, P. D.; Calero, G.; Ackerson, C. J.; Bushnell, D. A.; Kornberg, R. D. Structure of a Thiol Monolayer-Protected Gold Nanoparticle at 1.1 Å Resolution. *Science* **2007**, *318*, 430–433.
- (8) Bürgi, T. Properties of the Gold-Sulphur Interface: From Self-Assembled Monolayers to Clusters. *Nanoscale* **2015**, *7*, 15553–15567.
- (9) Jiang, D.; Tiago, M. L.; Luo, W.; Dai, S. The “Staple” Motif: A Key to Stability of Thiolate-Protected Gold Nanoclusters. *J. Am. Chem. Soc.* **2008**, *130*, 2777–2779.
- (10) Häkkinen, H. Atomic and Electronic Structure of Gold Clusters: Understanding Flakes, Cages and Superatoms from Simple Concepts. *Chem. Soc. Rev.* **2008**, *37*, 1847–1859.
- (11) Häkkinen, H.; Walter, M.; Grönbeck, H. Divide and Protect: Capping Gold Nanoclusters with Molecular Gold-Thiolate Rings. *J. Phys. Chem. B* **2006**, *110*, 9927–9931.
- (12) Aikens, C. M. Electronic Structure of Ligand-Passivated Gold and Silver Nanoclusters. *J. Phys. Chem. Lett.* **2011**, *2*, 99–104.
- (13) Walter, M. Ligand Protected Gold Alloy Clusters as Superatoms. In *High Performance Computing in Science and Engineering '10*; Springer Berlin Heidelberg: Berlin, Heidelberg, 2011; pp 29–41.
- (14) Reber, A. C.; Khanna, S. N. Superatoms: Electronic and Geometric Effects on Reactivity. *Acc. Chem. Res.* **2017**, *50*, 255–263.

- 1
2
3 (15) Nishigaki, J.; Koyasu, K.; Tsukuda, T. Chemically Modified Gold Superatoms and
4 Superatomic Molecules. *Chem. Rec.* **2014**, *14*, 897–909.
5
6 (16) Dognon, J.-P.; Clavaguéra, C.; Pyykkö, P. A Predicted Organometallic Series
7 Following a 32-Electron Principle: An@C₂₈ (An = Th, Pa⁺, U²⁺, Pu⁴⁺). *J. Am. Chem.*
8 *Soc.* **2009**, *131*, 238–243.
9
10 (17) Pyykkö, P.; Runeberg, N. Icosahedral WAu₁₂: A Predicted Closed-Shell Species,
11 Stabilized by Auophilic Attraction and Relativity and in Accord with the 18-Electron
12 Rule. *Angew. Chemie Int. Ed.* **2002**, *41*, 2174–2176.
13
14 (18) Li, J.; Li, X.; Zhai, H.-J.; Wang, L.-S. Au₂₀: A Tetrahedral Cluster. *Science* **2003**, *299*,
15 864–867.
16
17 (19) King, R. B.; Chen, Z.; Schleyer, P. von R. Structure and Bonding in the Omnicapped
18 Truncated Tetrahedral Au₂₀ Cluster: Analogies between Gold and Carbon Cluster
19 Chemistry. *Inorg. Chem.* **2004**, *43*, 4564–4566.
20
21 (20) Zubarev, D. Y.; Boldyrev, A. I. Deciphering Chemical Bonding in Golden Cages. *J.*
22 *Phys. Chem. A* **2009**, *113*, 866–868.
23
24 (21) Gruene, P.; Rayner, D. M.; Redlich, B.; van der Meer, A. F. G.; Lyon, J. T.; Meijer, G.;
25 Fielicke, A. Structures of Neutral Au₇, Au₁₉, and Au₂₀ Clusters in the Gas Phase.
26 *Science* **2008**, *321*, 674–676.
27
28 (22) Muñoz-Castro, A.; King, R. B. Au₂₀. Effect of a Strong Tetrahedral Field in a Spherical
29 Concentric Bonding Shell Model. *J. Phys. Chem. C* **2017**, *121*, 5848–5853.
30
31 (23) Wang, J.; Wang, G.; Zhao, J. Structures and Electronic Properties of Cu₂₀, Ag₂₀, and
32 Au₂₀ Clusters with Density Functional Method. *Chem. Phys. Lett.* **2003**, *380*, 716–720.
33
34 (24) Wang, Z. W.; Palmer, R. E. Direct Atomic Imaging and Dynamical Fluctuations of the
35 Tetrahedral Au₂₀ Cluster. *Nanoscale* **2012**, *4*, 4947–4949.
36
37 (25) Beletskaya, A. V.; Pichugina, D. A.; Shestakov, A. F.; Kuz'menko, N. E. Formation of
38 H₂O₂ on Au₂₀ and Au₁₉Pd Clusters: Understanding the Structure Effect on the Atomic
39 Level. *J. Phys. Chem. A* **2013**, *117*, 6817–6826.
40
41 (26) Aikens, C. M.; Schatz, G. C. TDDFT Studies of Absorption and SERS Spectra of
42 Pyridine Interacting with Au₂₀. *J. Phys. Chem. A* **2006**, *110*, 13317–13324.
43
44 (27) Manzoor, D.; Krishnamurthy, S.; Pal, S. Contriving a Catalytically Active Structure
45 from an Inert Conformation: A Density Functional Investigation of Al, Hf, and Ge
46 Doping of Au₂₀ Tetrahedral Clusters. *J. Phys. Chem. C* **2016**, *120*, 19636–19641.
47
48 (28) Cortés-Arriagada, D.; Oyarzún, M. P.; Sanhueza, L.; Toro-Labbé, A. Binding of
49
50
51
52
53
54
55
56
57
58
59
60

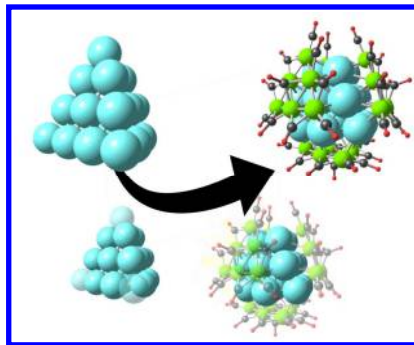
- 1
2
3 Trivalent Arsenic onto the Tetrahedral Au₂₀ and Au₁₉Pt Clusters: Implications in
4 Adsorption and Sensing. *J. Phys. Chem. A* **2015**, *119*, 6909–6918.
- 5
6 (29) Cortés-Arriagada, D.; Toro-Labbé, A. Insights into the Use of Au₁₉Cu and Au₁₉Pd
7 Clusters for Adsorption of Trivalent Arsenic. *Theor. Chem. Acc.* **2016**, *135*, 52.
- 8
9 (30) Tam, N. M.; Cuong, N. T.; Pham, H. T.; Tung, N. T. Au₁₉M (M=Cr, Mn, and Fe) as
10 Magnetic Copies of the Golden Pyramid. *Sci. Rep.* **2017**, *7*, 16086.
- 11
12 (31) Yuan, Y.; Cheng, L.; Yang, J. Electronic Stability of Phosphine-Protected Au₂₀
13 Nanocluster: Superatomic Bonding. *J. Phys. Chem. C* **2013**, *117*, 13276–13282.
- 14
15 (32) Zeng, C.; Liu, C.; Chen, Y.; Rosi, N. L.; Jin, R. Gold-Thiolate Ring as a Protecting
16 Motif in the Au₂₀(SR)₁₆ Nanocluster and Implications. *J. Am. Chem. Soc.* **2014**, *136*,
17 11922-11925.
- 18
19 (33) Zhang, H.-F.; Stender, M.; Zhang, R.; Wang, C.; Li, J.; Wang, L.-S. Toward the
20 Solution Synthesis of the Tetrahedral Au₂₀ Cluster. *J. Phys. Chem. B* **2004**, *108*,
21 12259–12263.
- 22
23 (34) Zeng, C.; Li, T.; Das, A.; Rosi, N. L.; Jin, R. Chiral Structure of Thiolate-Protected 28-
24 Gold-Atom Nanocluster Determined by X-Ray Crystallography. *J. Am. Chem. Soc.*
25 **2013**, *135*, 10011-10013.
- 26
27 (35) Weerawardene, K. L. D. M.; Aikens, C. M. Effect of Aliphatic versus Aromatic
28 Ligands on the Structure and Optical Absorption of Au₂₀(SR)₁₆. *J. Phys. Chem. C*
29 **2016**, *120*, 8354–8363.
- 30
31 (36) Longoni, G.; Chini, P. Carbonylnickelates. 2. Synthesis and Chemical Characterization
32 of the Dianion octadecylnonanickelate(2-). *Inorg. Chem.* **1976**, *15*, 3029–3031.
- 33
34 (37) Whoolery, A. J.; Dahl, L. F. Synthesis and Structural-Bonding Analysis of the
35 [Au₆Ni₁₂(CO)₂₄]²⁻ Dianion Containing an Unprecedented 18-Vertex Cubic Td Metal
36 Core Composed of Five Face-Fused Octahedra: The First Example of a Discrete
37 Gold/nickel Bimetallic-Bonded Species. *J. Am. Chem. Soc.* **1991**, *113*, 6683–6685.
- 38
39 (38) Whoolery Johnson, A. J.; Spencer, B.; Dahl, L. F. Synthesis and
40 Experimental/theoretical Investigation of the High-Nuclearity Cubic Td
41 [Au₆Ni₁₂(CO)₂₄]²⁻ Cluster, an Initial Example of a Discrete Gold-Nickel Bimetallic-
42 Bonded Species: Comparative Analysis of the Results of Electron-Counting Methods
43 and Th. *Inorganica Chim. Acta* **1994**, *227*, 269–283.
- 44
45 (39) Zhang, J.; Dahl, L. F. First-Known High-Nuclearity Silver–nickel Carbonyl Cluster:
46 Nanosized [Ag₁₆Ni₂₄(CO)₄₀]⁴⁻ Possessing a New 40-Atom Cubic Td Closed-Packed
47
48
49
50
51
52
53
54
55
56
57
58
59
60

- 1
2
3 Metal-Core geometry Dedicated by L. F. D. to Professor Dr. Wolfgang Beck, a Close
4 Friend, for His Many Remarkable Accom. *J. Chem. Soc. Dalton Trans.* **2002**, No. 7,
5 1269–1274.
6
7 (40) Andre Clayborne, P.; Häkkinen, H. The Electronic Structure of $\text{Ge}_9[\text{Si}(\text{SiMe}_3)_3]^{3-}$: A
8 Superantiatom Complex. *Phys. Chem. Chem. Phys.* **2012**, *14*, 9311–9316.
9
10 (41) Jena, P.; Khanna, S. N.; Rao, B. K. *Clusters and Nano-Assemblies*; WorldScientific:
11 Singapore, 2003.
12
13 (42) Ponce, I.; Silva, J. F.; Onate, R.; Rezende, M. C.; Paez, M. A.; Zagal, J. H.; Pavez, J.;
14 Mendizabal, F.; Miranda-Rojas, S.; Muñoz-Castro, A.; et al. Enhancement of the
15 Catalytic Activity of Fe Phthalocyanine for the Reduction of O_2 Anchored to Au (111)
16 via Conjugated Self-Assembled Monolayers of Aromatic Thiols As Compared to Cu
17 Phthalocyanine. *J. Phys. Chem. C* **2012**, *116*, 15329–15341.
18
19 (43) Wang, L.; Li, P.; Shi, H.; Li, Z.; Wu, K.; Shao, X. Thickness-Dependent Adsorption of
20 Melamine on Cu/Au(111) Films. *J. Phys. Chem. C* **2017**, *121*, 7977–7984.
21
22 (44) Ponce, I.; Silva, J. F.; Oñate, R.; Rezende, M. C.; Páez, M. A.; Pavez, J.; Zagal, J. H.
23 Enhanced Catalytic Activity of Fe Phthalocyanines Linked to Au (111) via Conjugated
24 Self-Assembled Monolayers of Aromatic Thiols for O_2 Reduction. *Electrochem.*
25 *commun.* **2011**, *13*, 1182–1185.
26
27 (45) Lin, C.-L.; Arafune, R.; Kawahara, K.; Tsukahara, N.; Minamitani, E.; Kim, Y.;
28 Takagi, N.; Kawai, M. Structure of Silicene Grown on Ag(111). *Appl. Phys. Express*
29 **2012**, *5*, 45802.
30
31 (46) Yasuda, S.; Kumagai, R.; Nakashima, K.; Murakoshi, K. Electrochemical Potential
32 Stabilization of Reconstructed Au (111) Structure by Monolayer Coverage with
33 Graphene. *J. Phys. Chem. Lett.* **2015**, *6*, 3403–3409.
34
35 (47) ADF Code, Vrije Universiteit, Amsterdam, The Netherlands, SCM,
36 [Http://www.scm.com](http://www.scm.com).
37
38 (48) Becke, A. D. Density-Functional Exchange-Energy Approximation with Correct
39 Asymptotic Behavior. *Phys. Rev. A* **1988**, *38*, 3098–3100.
40
41 (49) Perdew, J. P. Density-Functional Approximation for the Correlation Energy of the
42 Inhomogeneous Electron Gas. *Phys. Rev. B* **1986**, *33*, 8822–8824.
43
44 (50) Morokuma, K. Molecular Orbital Studies of Hydrogen Bonds. III. $\text{C}=\text{O}\cdots\text{H}-\text{O}$
45 Hydrogen Bond in $\text{H}_2\text{CO}\cdots\text{H}_2\text{O}$ and $\text{H}_2\text{CO}\cdots 2\text{H}_2\text{O}$. *J. Chem. Phys.* **1971**, *55* (3),
46 1236–1244.
47
48
49
50
51
52
53
54
55
56
57
58
59
60

- 1
2
3 (51) Ziegler, T.; Rauk, A. A Theoretical Study of the Ethylene-Metal Bond in Complexes
4 between copper(1+), silver(1+), gold(1+), platinum(0) or platinum(2+) and Ethylene,
5 Based on the Hartree-Fock-Slater Transition-State Method. *Inorg. Chem.* **1979**, *18*,
6 1558–1565.
7
8
9 (52) Bickelhaupt, F. M.; Baerends, E. J. Kohn-Sham Density Functional Theory: Predicting
10 and Understanding Chemistry. *Rev. Comput. Chem.*; K.B. Lipkowitz D.B. Boyd, Eds.;
11 Wiley, New York **2000**, *15*, 1–86.
12
13 (53) Perdew, J. P.; Burke, K.; Ernzerhof, M. Generalized Gradient Approximation Made
14 Simple. *Phys. Rev. Lett.* **1996**, *77*, 3865–3868.
15
16 (54) Lopez-Acevedo, O.; Akola, J.; Whetten, R. L.; Grönbeck, H.; Häkkinen, H. Structure
17 and Bonding in the Ubiquitous Icosahedral Metallic Gold Cluster Au₁₄₄ (SR) 60. *J.*
18 *Phys. Chem. C* **2009**, *113*, 5035–5038.
19
20 (55) Akola, J.; Walter, M.; Whetten, R. L.; Häkkinen, H.; Grönbeck, H. On the Structure of
21 Thiolate-Protected Au₂₅. *J. Am. Chem. Soc.* **2008**, *130*, 3756–3757.
22
23 (56) Akola, J.; Kacprzak, K. A.; Lopez-Acevedo, O.; Walter, M.; Grönbeck, H.; Häkkinen,
24 H. Thiolate-Protected Au₂₅ Superatoms as Building Blocks: Dimers and Crystals. *J.*
25 *Phys. Chem. C* **2010**, *114*, 15986–15994.
26
27 (57) Jiang, D.; Kühn, M.; Tang, Q.; Weigend, F. Superatomic Orbitals under Spin-Orbit
28 Coupling. *J. Phys. Chem. Lett.* **2014**, *5*, 3286–3289.
29
30 (58) Gam, F.; Paez-Hernandez, D.; Arratia-Perez, R.; Liu, C. W.; Kahlal, S.; Saillard, J.-Y.;
31 Muñoz-Castro, A. Coinage Metal Superatomic Cores: Insights into Their Intrinsic
32 Stability and Optical Properties from Relativistic DFT Calculations. *Chem. - A Eur. J.*
33 **2017**, *23*, 11330–11337.
34
35 (59) Longoni, G.; Manassero, M.; Sansoni, M. Synthesis and Structural Characterization of
36 Bimetallic Iron-Platinum Carbonyl Clusters: Their Relationship with Bimetallic Iron-
37 Palladium Carbonyl Clusters. *J. Am. Chem. Soc.* **1980**, *102*, 7973–7974.
38
39 (60) Adams, R. D.; Chen, G.; Wang, J.-G. Platinum-Iron Carbonyl Cluster Complexes. The
40 Synthesis and Structural Characterizations of Pt₃Fe₃(CO)₁₅ and Pt₅Fe₂(CO)₁₂(COD)₂.
41 *Polyhedron* **1989**, *8*, 2521–2523.
42
43 (61) Adams, R. D.; Arafa, I.; Chen, G.; Lii, J. C.; Wang, J. G. New Platinum-Iron Carbonyl
44 Cluster Complexes and Their Reactions with Alkynes. *Organometallics* **1990**, *9*, 2350–
45 2357.
46
47 (62) Evans, D. G.; Mingos, D. M. P. Polyhedral Skeletal Electron Pair Theory - Its
48
49
50
51
52
53
54
55
56
57
58
59
60

1
2
3 Extension to Nonconical Fragments. *Organometallics* **1983**, 2, 435–447.
4
5
6
7
8
9
10
11
12
13
14
15
16
17
18
19
20
21
22
23
24
25
26
27
28
29
30
31
32
33
34
35
36
37
38
39
40
41
42
43
44
45
46
47
48
49
50
51
52
53
54
55
56
57
58
59
60

TOC graphics



A rationalization of T_d $[M_{16}Ni_{24}(CO)_{40}]^{4+}$ ($M = Cu, Ag, Au$), reveals strong analogy with the landmark Au_{20} cluster, on the basis of a common 20-*ve* $[M_{16}]^{4+}$ core. Thus, further chemistry can be developed for a $M(111)$ finite surface section of Group 11 elements.